Cross-section measurement of two-photon in-flight annihilation of positrons at $\sqrt{s} = 20$ MeV with the PADME detector

F. Bossi,[1] P. Branchini,[2] B. Buonomo,[1] V. Capirossi,[3] A. P. Caricato,[4,5] G. Chiodini,[4] R. De Sangro,[1] C. Di Giulio,[1] D. Domenici,[1] F. Ferrarotto,[6] G. Finocchiaro,[1] L. G. Foggetta,[1] A. Frankenthal,[7] M. Garattini,[1] G. Georgiev,[8,9] F. Giacchino,[1,†] P. Gianotti,[1] S. Ivanov,[9] Sv. Ivanov,[9] V. Kozhuharov,[9,1] E. Leonardi,[6] E. Long,[10,6] M. Martino,[4,5] I. Oceano,[4,5,*] F. Oliva,[4,5,‡] G. C. Organtini,[10,6] F. Pinna,[3] G. Piperno,[10] M. Raggi,[10,6] I. Sarra,[1] R. Simeonov,[9] T. Spadaro,[1] S. Spagnolo,[4,5] E. Spiriti,[1] D. Tagnani,[2] C. Taruggi,[1] P. Valente,[6] and E. Vilucchi[1]

[1]*INFN Laboratori Nazionali di Frascati, via E. Fermi 54, Frascati 00044, Italy*
[2]*INFN Sezione Roma 3, via della vasca navale 84, Roma 00146, Italy*
[3]*DISAT Politecnico di Torino and INFN Sezione Torino, C.so Duca degli Abruzzi 24, Torino 10129, Italy*
[4]*INFN Sezione Lecce, via Provinciale per Arnesano, Lecce 73100, Italy*
[5]*Dipartimento di Matematica e Fisica Salento Università, via Provinciale per Arnesano, Lecce 73100, Italy*
[6]*INFN Sezione Roma 1, p.le A. Moro 2, Rome 00185, Italy*
[7]*Physics Department, Princeton University, Washington Road, Princeton, New Jersey 08540, USA*
[8]*INRNE Bulgarian Accademy of Science, 72 Tsarigradsko shosse Boulevard, Sofia 1784, Bulgaria*
[9]*Faculty of Physics, Sofia Università "St. Kl. Ohridski", 5J. Bourchier Boulevard, Sofia 1164, Bulgaria*
[10]*Dipartimento di Fisica Sapienza Università, p.le A. Moro 2, Roma 00185, Italy*

(Received 8 November 2022; accepted 20 December 2022; published 30 January 2023)

A measurement of the inclusive cross section of in-flight electron-positron annihilation to photons, $e^+e^- \to \gamma\gamma$, is presented using the PADME detector at the Laboratori Nazionali di Frascati. A beam of 430 MeV positrons, corresponding to a center-of-mass energy of 20 MeV, strikes a thin diamond target. The two photons produced in the interaction are detected by an electromagnetic calorimeter made of BGO crystals. The measurement is the first based on direct detection of the photon pair and one of the most precise for positron energies below 1 GeV. It represents an intermediate step in the ultimate PADME goal of searching for dark sector particles and mediators weakly coupled to photons and electrons, with masses ranging from 1 to 20 MeV. The final value, $\sigma_{e^+e^-\to\gamma\gamma} = (1.977 \pm 0.018(\text{stat}) \pm 0.119(\text{syst}))$ mb, agrees with next-to-leading-order QED predictions within the 6% experimental uncertainty.

DOI: 10.1103/PhysRevD.107.012008

I. INTRODUCTION

PADME (Positron Annihilation into Dark Matter Experiment) at the Laboratori Nazionali di Frascati (LNF) of INFN is a fixed-target experiment designed to search for a hypothetical dark photon A' produced in association with a photon in electron-positron annihilation [1] using a beam of positrons. This particle is postulated to be the gauge boson associated with a $U_d(1)$ symmetry in a sector where dark matter would be confined according to the paradigm of "hidden-sector" theoretical models [2]. A simple model allowing very weak interactions of standard model (SM) particles with dark matter is obtained by kinetic mixing [3].

PADME is expected to be sensitive to the kinetic mixing coefficient ϵ, describing the effective coupling between A' and the photon, relative to the electromagnetic coupling α, for $\epsilon \geq 10^{-3}$ and values of the A' mass $m_{A'} \leq 23.7$ MeV after collecting $\approx 10^{13}$ positrons-on-target (POT) at the energy of 550 MeV. The search technique relies on the reconstruction of the squared missing mass $M^2 = (P_{e^+} + P_{e^-} - P_\gamma)^2$ of single-photon final states. In this expression, the positron four-momentum P_{e^+} is determined by the PADME beamline (see Sec. II A). The photon four-momentum P_γ is measured by a high-resolution segmented electromagnetic calorimeter (ECAL), based on the position of the beam spot on the target, where positrons are assumed

*Corresponding author.
isabella.oceano@le.infn.it
†Present address: INFN Sezione Roma 2, via della Ricerca Scientifica 1, Rome, Italy.
‡Present address: School of Physics and Astronomy, Edinburgh University, Edinburgh, United Kingdom.

to annihilate with electrons at rest ($P_{e^-} \ll P_{e^+}$). Therefore, understanding the ECAL performance via the study of the theoretically well-known QED process of electron-positron annihilation to photons $e^+e^- \to \gamma\gamma$ is a crucial intermediate step in the ultimate physics goal of the experiment. The measurement of this cross section allows for the calibration of photon reconstruction and for the monitoring of the beam intensity with high precision.

A few measurements of the $e^+e^- \to \gamma\gamma$ cross section were performed in the second half of the 1950s, exploiting the disappearance of positron tracks in a target. Colgate and Gilbert in 1953 provided measurements with a precision of about 20% by determining the attenuation of positrons with energies of 50, 100 and 200 MeV [4]. In 1963, Malamud and Weill reached a precision of about 4% using a bubble chamber and positrons accelerated to an energy of 600 MeV [5]. In 1962, Fabiani *et al.* measured the annihilation cross section for positrons with energies of 1.94, 5.80, 7.71, and 9.64 GeV at CERN, reaching an uncertainty better than about 5% [6].

This paper presents the first direct measurement of the absolute cross section of annihilation in flight to photons of 430 MeV positrons. Section II describes the PADME beam and detector, along with the photon reconstruction technique. Section III presents the data used in the measurement and the event selection. The measurement strategy is detailed in Sec. IV along with the main uncertainties and results. The selection requirements are designed to be inclusive of events with extra radiation. The measurement is therefore compared to the QED prediction at the next-to-leading-order (NLO) approximation for the inclusive $e^+e^- \to \gamma\gamma(\gamma^*)$ cross section.

II. THE PADME EXPERIMENT

A. The positron beam

The PADME experiment, showed in Fig. 1, is located in the BTF (Beam Test Facility) of the Laboratori Nazionali di Frascati where the LINAC of the DAΦNE collider provides a variable energy positron beam [7,8]. Upstream of the last bending dipole, a 125 μm thick mylar window separates the LINAC high vacuum region from the PADME vacuum region, where less stringent conditions are required. The data used for this analysis were collected from September to November 2020 with a beam energy of about 430 MeV and an average beam intensity of 27×10^3 positrons, approximately evenly distributed in 250 ns long bunches. This data-taking period is referred to as the Padme Run II.

1. The diamond active target

The diamond active target [9] provides estimates of the particle multiplicity in the bunch and the average position of the beam interaction point. It is a full carbon doubled-sided strip detector 100 μm thick and with an area of 2×2 cm^2 made of CVD (chemical vapour deposition) polycrystalline diamond. A pattern of graphite strip electrodes, obtained by irradiation with an ArF laser, measures coordinates in orthogonal directions on the two sides. The thickness of the graphite strips was estimated to be about 200 nm, with negligible material ablation. Sixteen electrodes per side were connected to the front-end electronics.

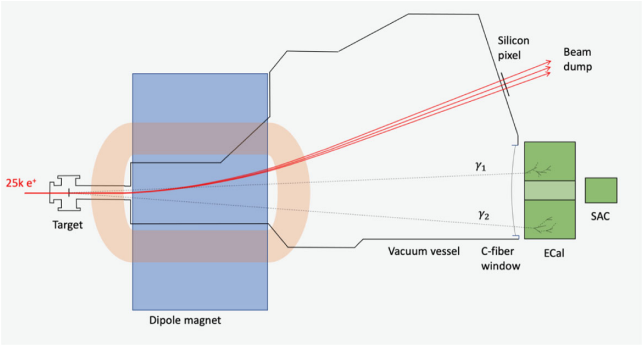

FIG. 1. Schematic view of the PADME experiment showing the components relevant to the $e^+e^- \to \gamma\gamma$ cross-section measurement.

The target sits in the beam pipe vacuum. A remotely controlled step-motor is used to move it out of the beam and park it on the side when collecting special data for studies of beam-related backgrounds (which do not originate from particle interactions with the target).

B. The electromagnetic calorimeter

The main detector of the PADME experiment is the electromagnetic calorimeter (ECAL) [10]. It is a segmented calorimeter made of 616 BGO crystals. The dimensions of each crystal are $2.1 \times 2.1 \times 23$ cm^3, to fully contain the electromagnetic shower in the longitudinal direction and about 70% of it in the transverse direction. The crystals are arranged in a cylindrical array with a central square hole, corresponding to 5×5 missing crystals, and an external radius of 30 cm. The hole prevents the calorimeter from being overwhelmed by the high rate of bremsstrahlung photons emitted in the forward direction. The scintillation light is detected by HZC XP1911 type B photomultipliers (19 mm diameter) [10], which have a maximum quantum efficiency of about 21% at 480 nm, where the light emission of BGO is also maximized. The BGO light emission intensity changes with temperature by about 0.9%/°C. Hence the ECAL temperature map is monitored with 40 Pt1000 probes to ensure temperature stability.

For each beam bunch impinging on the target, the signals of all photomultipliers are digitized [11] in a readout window 1 μs wide at the rate of 1 Gs/s with 12-bit ADCs. The waveforms are recorded after zero suppression. A cosmic ray trigger was setup to collect data for continuous monitoring of the gain during data taking. These data were also used to estimate the average channel efficiency, which was found to be about 99.6% for cosmic rays [12].

C. Photon reconstruction

The reconstruction of photons in the ECAL is based on waveform processing, allowing for the reconstruction of up to three hits per crystal, where a hit is defined as the energy deposition of a single particle. The algorithm uses a signal template derived from data. The energy and time of a hit is estimated from the scale and shift factors of the template required to adjust it to a given pulse in the waveform. The algorithm accounts for waveforms with a truncated tail, due to the limited time acquisition window, or with a saturated amplitude, due to large energy deposition or overlapping particles. The hit energies are corrected by relative calibration factors extracted from the cosmic ray data sample. An additional absolute calibration factor is applied to match the average total energy of annihilation photon pairs to the beam energy.

Hits close in time and space are grouped in clusters not larger than 7×7 crystals. The clustering procedure starts from a seeding hit with energy of at least 20 MeV. All nearby hits with energy above 1 MeV at a distance from the seed not exceeding three crystals and in time coincidence within 6 ns are merged. The cluster energy is given by the sum of the energies of all constituent hits. Transverse position and time are given by energy-weighted averages.

III. DATA SAMPLE AND EVENT SELECTION

A. Data and Monte Carlo simulation samples

The data used for this measurement were collected during the PADME Run II. The positron beam energy was stable at 432.5 MeV, with a relative energy spread of 0.5% and a typical particle density in the bunch of about 100 POT/ns. They correspond to a subset of the data featuring good stability in beam spot intensity and position on the target during the run. The main features of these runs are summarized in Table I. The total number of POT, after event quality cuts (see Sec. III B), amounts to 3.97×10^{11}, with an expected yield of two-photon annihilation events of about 5×10^5. Therefore, this dataset allows for a measurement with a statistical error smaller than 1%.

TABLE I. Main features of the runs used in this analysis.

Run	N_{POT} $[10^{10}]$	e^+/bunch $[10^3]$	Bunch length (ns)
30369	8.2	27.0 ± 1.7	260
30386	2.8	19.0 ± 1.4	240
30547	7.1	31.5 ± 1.4	270
30553	2.8	35.8 ± 1.3	260
30563	6.0	26.8 ± 1.2	270
30617	6.1	27.3 ± 1.5	270
30624	6.6	29.5 ± 2.1	270
30654	No target	~27	~270
30662	No target	~27	~270

Special runs were collected with the target out of the beam to study the background component unrelated to beam-target interactions, which we refer to as beam background. This component originates from out-of-orbit positrons as well as positrons radiating when crossing the mylar vacuum separation window. These particles can interact with beamline elements and produce showers of secondary particles, occasionally reaching the detectors [13].

The experiment was simulated with the GEANT4 software [14]. The positron beam is generated just upstream of the target, with bunch multiplicity of 25×10^3, Gaussian spot of 1 mm, divergence of 0.1 mrad, and energy spread of 1 MeV. The dominant QED processes are simulated according to the GEANT4 physics list, including bremsstrahlung (on nuclei and atomic electrons), annihilation, Bhabha scattering, and other subdominant processes. Therefore, the simulation reproduces the effects of pile-up positron interactions in the target, resulting in several overlapping photons in the calorimeter within the same bunch (a full PADME event). It does not, however, describe the beam background. A simulation of the beamline was also available but not used in this work, where data-driven techniques were preferred to estimate the impact of such background on the analysis sensitivty.

Signal acceptance and event migration induced by resolution effects are most conveniently estimated from simulations of single-annihilation events, free from pile-up and with the true photon kinematics readily accessible. The CalcHEP generator [15] at leading order (LO) and the Babayaga generator [16,17] at LO and NLO were used to generate the kinematics of annihilation events. For certain samples, the final-state photons were added to the GEANT4 simulation event-by-event, choosing a production vertex corresponding to a location in the target reached by an incoming beam positron. The positron tracking was then stopped, thus emulating its annihilation in flight, and the photons were propagated through the detectors like any other primary or secondary simulated particle.

A summary of the main features of the Monte Carlo simulation samples is reported in Table II.

TABLE II. Monte Carlo simulation samples used in the analysis. Each sample contains 10^6 events.

Generator	Process	Approximation
GEANT4	e^+ Bremsstrahlung	LO
	$e^+e^- \to \gamma\gamma$	LO
	$e^+e^- \to e^+e^-$	LO
CalcHEP	$e^+e^- \to \gamma\gamma$	LO
CalcHEP + GEANT4	$e^+e^- \to \gamma\gamma$ (1 e^+/bunch)	LO
CalcHEP + GEANT4	$e^+e^- \to \gamma\gamma$ (25000e^+/bunch)	LO
Babayaga	$e^+e^- \to \gamma\gamma$	LO
Babayaga	$e^+e^- \to \gamma\gamma(\gamma)$	NLO

B. Event and photon selection

An event pre-selection was obtained considering only bunches where the number of POT measured by the active target was less than $\pm 5\sigma$ away from the average. This condition rejects uninteresting events, such as cosmic triggers and empty bunches, bunches with anomalous high multiplicity, and any accidental mismeasurement of the number of POT by the target.

Several requirements were applied to the ECAL clusters to obtain a clean sample of annihilation photons: cluster position offset from the crystal seed position smaller than 20 mm, standard deviation of the x and y coordinates of hits in the cluster greater than 1 mm, standard deviation of the arrival time of hits in the cluster lower than 3 ns, and linear correlation between x and y coordinates of cluster hits weighted by energy lower than 0.99. In addition, an isolation cut was applied, rejecting all in-time clusters (within 10 ns) that presented a second cluster closer than 200 mm. These criteria reduced the number of clusters considered in the analysis by 50% on average, while clusters from genuine annihilation photons were accepted with an efficiency of 90%. The cluster quality cuts significantly reduce the systematic errors on the two-photon yields (see Sec. IV B).

C. $e^+e^- \to \gamma\gamma$ kinematics

To describe the kinematics, we use the following coordinate system. The polar angle θ is defined as the angle between the photon direction and the z axis of the PADME reference frame, which corresponds to the direction of the incoming positron beam. The azimuthal angle ϕ is the angle between the direction of a photon projected in the plane perpendicular to the beam and the horizontal x axis. The y axis is vertical and upward.

In the Born approximation, the two-photon kinematics of the e^+e^- annihilation process is highly constrained, implying the following relations:

(i) The sum of the energies of the two photons is equal to the beam energy: $E_{\gamma_1} + E_{\gamma_2} = E_{\text{beam}}$;

(ii) The photon momenta are back-to-back in the transverse plane: $\phi_{\gamma_1} - \phi_{\gamma_2} = \pi$;

(iii) For each photon, the polar angle is a function of the energy: $E_{\gamma_i} = f(\theta_{\gamma_i})$;

(iv) The center-of-gravity (CoG) of the interaction in the transverse plane is zero, where the CoG is defined by

$$CoG_{x(y)} = \frac{x(y)_{\gamma_1} E_{\gamma_1} + x(y)_{\gamma_2} E_{\gamma_2}}{E_{\gamma_1} + E_{\gamma_2}}; \qquad (1)$$

(v) The "squared missing mass" is close to zero for each photon, which is defined as the invariant mass of the system produced with the photon in the e^+e^- annihilation:

$$M^2_{\text{miss}} = 2m_e \left[E_{\text{beam}} - E_\gamma \left(1 + \frac{E_{\text{beam}}}{2m_e} \theta^2_\gamma \right) \right]. \qquad (2)$$

For a given beam energy, the previous relations imply that whenever the energy or the polar angle of one annihilation photon in the pair is measured, the energy and polar angle of the other annihilation photon can be predicted. The relations are used in data to calibrate the ECAL energy response and to verify its assembly geometry and alignment with respect to the real beam axis and target spot.

In Fig. 2, the energy sum of two good quality ECAL clusters in time coincidence (within 10 ns) is shown for data after ECAL energy calibration (see Sec. II C).

Figure 3 shows distributions of the x and y coordinates of the CoG of a pair of good quality clusters in time coincidence within 10 ns. These are obtained after applying event-by-event x and y shifts of the ECAL cluster positions to correct for a global ECAL offset with respect to the beamline ($x_{\text{ECAL}} = -3.13$ mm and $y_{\text{ECAL}} = -3.86$ mm, confirmed by survey measurements), and for run-dependent offsets (of the order of 1 mm) due to small changes of the beam position and direction, confirmed by the active target beam spot monitor.

In Fig. 4 the correlation between the radial position R_{γ_1} of the most energetic photon and the radial position R_{γ_2} of the other photon in the pair (which are each strictly correlated to the corresponding polar angles θ_{γ_i}) is shown for the LO CalcHEP generator and for annihilation event candidates in data.

In Fig. 5 the correlation between energy E and radial position R of each photon is shown for the LO CalcHEP generator and for annihilation event candidates in data after energy calibration and CoG correction. In simulation, the radial photon position in the ECAL is computed as $R_\gamma = D\sqrt{p_x^2 + p_y^2}/p_z$ in terms of the momentum components

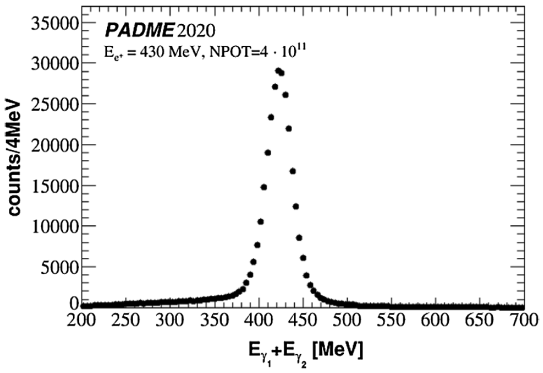

FIG. 2. Sum of the energies of the two-photon candidates. The mean and standard deviation of the distribution core are 422.9 MeV and 14.8 MeV, respectively.

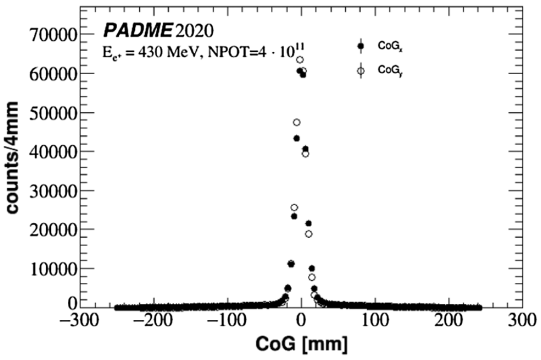

FIG. 3. The CoG of the interaction in the x and y direction, reconstructed from two-photon candidates, after applying run-dependent corrections. The mean and standard deviation of the distribution core are −0.38 mm and 7.61 mm in the x view, and −0.84 mm and 7.24 mm in the y view.

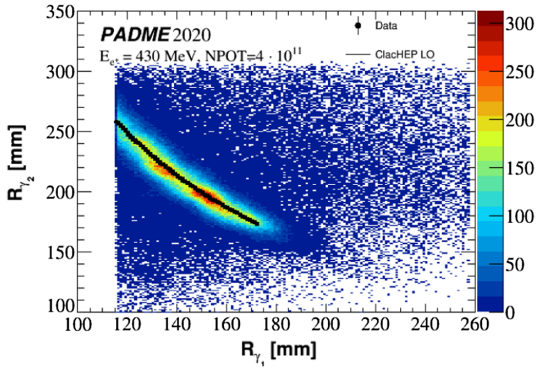

FIG. 4. Scatter plot between the radial positions of the leading and subleading photons with data (black points) and CalcHEP LO (colored points).

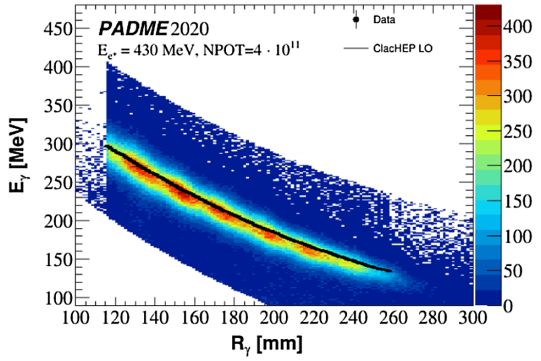

FIG. 5. Scatter plot between energy and radial positions of each photon with data (black points) and CalcHEP LO (colored points).

(p_x, p_y, p_z) and D, which is defined as the distance of the ECAL front surface from the target ($D_{\mathrm{ECAL}} = 3470$ mm) plus the average electromagnetic shower depth, as predicted by the PADME simulation ($\Delta z_{\mathrm{shower}} = 73$ mm). With this truth definition, the deviation between the $E(R)$ correlation in data and simulation is less than 1% over the range of interest. This agreement reveals the accuracy of the geometrical parameters describing the ECAL crystal array in data reconstruction and the overall ECAL alignment. For this geometry cross-check, a tight selection of photon pairs reconstructed in a fiducial region of the ECAL was used.

IV. INCLUSIVE $e^+e^- \to \gamma\gamma$ PRODUCTION CROSS SECTION

The cross section is determined as follows:

$$\sigma_{e^+e^-\to\gamma\gamma} = \frac{N_{e^+e^-\to\gamma\gamma}}{N_{\mathrm{POT}} \cdot n_{e/S} \cdot A_g \cdot A_{\mathrm{mig}} \cdot \epsilon_{e^+e^-\to\gamma\gamma}}, \quad (3)$$

where:

(i) $N_{e^+e^-\to\gamma\gamma}$ is the signal yield;

(ii) $N_{\mathrm{POT}} = (3.97 \pm 0.16) \times 10^{11}$ is the total number of positrons on target as determined by the active diamond target. It corresponds to the integral of the number of POT estimated event-by-event by the target;

(iii) $n_{e/S} = \rho N_A dZ/A = 0.01025 \pm 0.00038$ b^{-1} is the electron surface density of the target, where $\rho = 3.515 \pm 0.015$ g/cm^3 is the diamond density, Z and A are the carbon atomic number and weight, respectively, and $d = (0.0969 \pm 0.0036)$ mm is the estimated average diamond target thickness;

(iv) A_g is the acceptance of the selection, determined by the ECAL geometry;

(v) A_{mig} is a correction factor for event migration across the boundaries of the acceptance region;

(vi) $\epsilon_{e^+e^-\to\gamma\gamma}$ is the combined detection, reconstruction and selection efficiencies for two-photon events within acceptance.

A. Two-photon selection

A fiducial region defined by 115.82 mm $< R_{\gamma_{1(2)}} <$ 258 mm is introduced to enforce a reliable photon reconstruction. The corresponding range of photon polar angles is [32.75, 72.74] mrad. Clusters in this region are at a distance from the inner and outer boundaries of the calorimeter equal to at least twice the size of a BGO crystal. This ensures good transverse shower containment and, therefore, good determination of the energy and position. The edge values of this region are chosen to be consistent with the two-photon kinematics. The radial position where the two photons have equal energy, $R_{\mathrm{mid}} = 172.83$ mm ($\theta_{\mathrm{mid}} = 48.78$ mrad), is determined from data and found to be consistent with the LO simulation at the generator level. This is used to define the inner and outer rings of the fiducial region for efficiency measurements and yield determination based on a single-photon selection.

The event selection applied for the measurement of the inclusive $e^+e^- \to \gamma\gamma$ cross section requires two photons matching the following criteria:

(i) Time coincidence $|t_{\gamma_1} - t_{\gamma_2}| < 10$ ns;
(ii) Photon energy $E_{\gamma_{1(2)}} > 90$ MeV;
(iii) Energy and polar angle consistency for each photon: $|\Delta E_i| = |E_{\gamma_i} - f(\theta_i)| < 100$ MeV;
(iv) Radial position of the most energetic photon (γ_1) in the fiducial region 115.82 mm $< R_{\gamma_1} <$ 258 mm.

The fiducial region constraint, although applied explicitly only to the leading photon, in practice holds also for the second photon (for a large majority of two-photon events, where limited radiative effects are seen) and it defines an energy threshold for both photons well above the lower limit explicitly enforced by the selection. Indeed, this requirement is the only criterion defining the acceptance of the event selection. The remaining requirements are very loose compared to the detector resolution. Therefore, acceptance and efficiency do not strongly depend on detailed features of the detector that might be difficult to simulate at the percent level as required by the statistical precision of the analysis.

B. Two-photon annihilation yield

The two-photon annihilation yield is estimated from the distribution of the observable

$$\Delta\phi = \phi_{\gamma_1} - \phi_{\gamma_2} - \pi, \tag{4}$$

which is symmetric around zero and features a reasonably flat background. Figure 6 shows the $\Delta\phi$ distribution over the entire dataset of the analysis. Here the fitting function is the sum of two Gaussian distributions for the signal and a second-order polynomial for the background. After background subtraction, which contaminates the selection by less than 10%, the total number of annihilation events available for the cross-section measurement is 276700 ± 560.

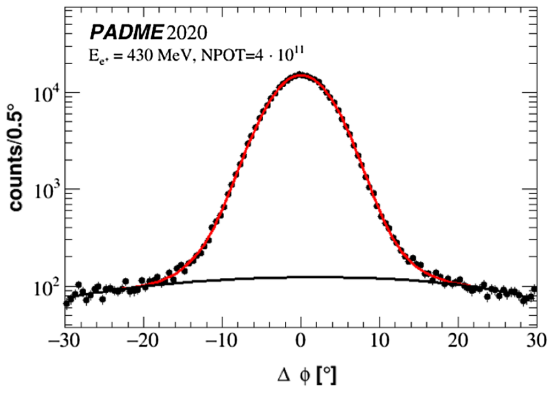

FIG. 6. Deviation from 180° of the azimuthal angle difference between the two-annihilation photons candidates.

The annihilation yield is also measured in eight azimuthal ECAL slices, each 45° wide, by assigning each photon-pair candidate to the slice where the leading photon is reconstructed. The subleading photon in the pair lies in the opposite slice, or just across its borders due to resolution effects.

The annihilation yield has also been measured with a single-photon selection by looking for photons fulfilling kinematic conditions specific of annihilation photons, like $\Delta E \sim 0$ MeV or $M^2_{\text{miss}} \sim 0$ MeV. The cross section is still computed according to Eq. (3) with the efficiency being, in this case, the single-photon efficiency.

C. Acceptance

The acceptance is defined by the range allowed for the radial position of the leading photon using Babayaga at NLO, which consistently treats final states with two or three photons. It was determined as the fraction of generated events satisfying: at least two photons with energy above 90 MeV; $|E_\gamma - f(\theta_\gamma)| < 100$ MeV; and the leading photon located in the radial fiducial region. Photons separated at the ECAL surface by a distance smaller than the clusterization distance were merged. The acceptance value determined in this way is 0.06368 ± 0.00025, where the error is statistical. This is 1.6% lower than the acceptance estimated at LO. At LO, the predictions from Babayaga and CalcHEP agree within 0.4%.

Finally, the contribution to the systematic error on the cross-section measurement due to the acceptance cut was estimated by varying the inner edge of the radial fiducial region by up to ± 0.5 mm, corresponding to the estimated error on the alignment from detector surveys. The resulting relative uncertainty on the cross-section measurement was found to be 1.16%.

D. Event migration effects

In Eq. (3) the effect of event migration across the boundaries of the acceptance, induced by limited detector resolution, is corrected with the factor A_{mig}. Given the definition of acceptance discussed in Sec. IV C, this is due to the migration of the leading photon in the event across the inner edge of the radial fiducial region, caused either by resolution effects or by biases in the measurement of the cluster position.

The sample of $e^+e^- \to \gamma\gamma$ events generated with CalcHEP at LO was simulated ignoring dead channels in the calorimeter and any sources of physics or beam-related background. As a consequence, the distributions of energies and positions of the photons reconstructed with the same algorithm applied in data are representative of the true distributions, convolved with resolution effects, with negligible inefficiency. The correction A_{mig} was computed as the ratio between the number of events with the leading photon reconstructed at a radius $R \geq R_{\text{min}}$ and the number

of events with the leading photon satisfying the same condition at generator level. The result is $A_{\mathrm{mig}} = 0.996 \pm 0.003$, where the systematic error reported is a conservative estimate of variations induced by an imperfect knowledge of the inner boundary of the acceptance region or by a mismatch of the reconstructed radial position profile between data and simulation due to mismodeling of the detector resolution.

E. Reconstruction efficiency

The overall single photon efficiency ϵ_γ was measured in data with a tag-and-probe technique, exploiting the closed kinematics of two-photon annihilation events.

For annihilation photons, or tags, the variable $\Delta E_{\mathrm{tag}} = E_{\mathrm{tag}} - f(\theta_{\mathrm{tag}})$, where E_{tag} is the measured energy and $f(\theta_{\mathrm{tag}})$ the expected energy, must be approximately zero. This feature can be used to identify tag candidates. Each tag can be correlated to a second photon, or probe, with opposite azimuthal angle $\phi_{\mathrm{probe}} = \phi_{\mathrm{tag}} + \pi$, energy $E_{\mathrm{probe}} = E_{\mathrm{beam}} - E_{\mathrm{tag}}$, and satisfying $\Delta E_{\mathrm{probe}} = E_{\mathrm{probe}} - f(\theta_{\mathrm{probe}}) \approx 0$ MeV. A cluster passing all photon selection requirements that has features matching those of the probe is labeled a "matched probe" and considered efficiently reconstructed. Unmatched probes correspond instead to an inefficiency for a photon with $\phi = \phi_{\mathrm{probe}}$ and $R = R_{\mathrm{probe}}$ (or $E = E_{\mathrm{probe}}$).

The efficiency ϵ_γ has been evaluated in 16 bins corresponding to eight azimuthal angle slices (each 45° wide) times two radial regions, the inner one ranging from R_{min} to R_{mid}, and the outer one from R_{mid} to R_{max}.

The efficiency $\epsilon_\gamma(i,j)$ in a generic bin identified by the index i, ranging over the eight azimuthal slices, and the index j, ranging over the two radial bins, is estimated as the fraction of probes predicted in that bin by tags reconstructed in the opposite radial and azimuthal bin, which are actually matched by reconstructed (and selected) photons, i.e.

$$\epsilon_\gamma(i,j) = N_{\mathrm{matched-probes}}(i,j)/N_{\mathrm{tag}}(i',j'). \qquad (5)$$

The number of tags in a given bin, $N_{\mathrm{tag}}(i',j')$, is obtained from a fit to the ΔE_{tag} distribution of all photons passing the following tag selection:

(i) $E_{\mathrm{tag}} > 90$ MeV;
(ii) $|\Delta E_{\mathrm{tag}}| < 100$ MeV.

The fitting model is the sum of two Gaussian distributions for the signal (with total yield $\mathrm{N_{tag}}$) and two background templates. All signal and background components have fixed shape and floating amplitudes. The background originates from different sources, such as physics backgrounds from in-time interactions, and beam-related backgrounds. The shape of the first component is extracted from a Monte Carlo simulation sample with pile-up (mostly bremsstrahlung), which is representative of interactions in the target. The shape of the second component is extracted from no-target data, which are representative of interactions in the detector and beamline materials (except the target and its support). The relative fraction of the two background components in data strongly depends on the azimuthal and radial position. The ΔE_{tag} distribution of all photons in the inner radial region $R_{\mathrm{min}} < R_{\mathrm{tag}} < R_{\mathrm{mid}}$ passing the tag selection is shown in Fig. 7.

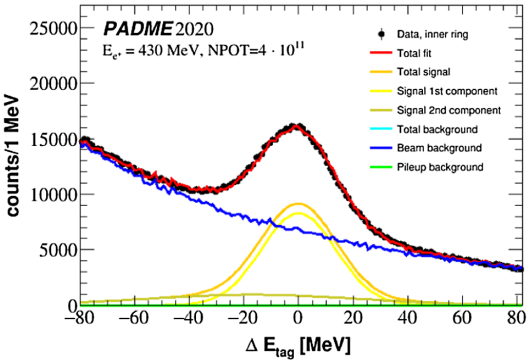

FIG. 7. Distribution of the ΔE_{tag} observable for all photons in the inner ring of the radial fiducial region passing the tag selection.

The number of matched probes in a given bin, $N_{\mathrm{matched-probes}}(i,j)$, is estimated from the distribution of $\Delta E'_{\mathrm{probe}} = E_{\mathrm{probe}} - E_{\mathrm{beam}} + f(\theta_{\mathrm{tag}})$ for all pairs consisting of a tag-photon in the opposite bin, and a matched-probe photon passing the following selection criteria:

(i) $\phi_{\mathrm{tag}} \in$ bin i' and $R_{\mathrm{tag}} \in$ bin j';
(ii) $|\phi_{\mathrm{tag}} + \pi - \phi_{\mathrm{probe}}| < 25°$;
(iii) $|t_{\mathrm{probe}} - t_{\mathrm{tag}}| < 7$ ns and $E_{\mathrm{probe}} > 90$ MeV;
(iv) $|\Delta E_{\mathrm{probe}}| < 100$ MeV and $|\Delta E'_{\mathrm{probe}}| < 100$ MeV.

If more than one matched probe is found for a given tag, the photon with the minimum value of $(\Delta E'_{\mathrm{probe}})^2 + (\Delta E_{\mathrm{probe}})^2$ is selected. The background in the $\Delta E'_{\mathrm{probe}}$ distribution is estimated with a template, obtained in no-target data, of fixed shape and amplitude. The template is constrained by matching the yield of the scaled no-target template to target data in the left side-band, $[-150, -90]$ MeV. The background of the matched probe distribution is quite small, and thus the contribution from pile-up is negligible. Figure 8 shows the $\Delta E'_{\mathrm{probe}}$ distribution and the scaled no-target data of all photons within the outer radial region $R_{\mathrm{mid}} < R_{\mathrm{tag}} < R_{\mathrm{max}}$ passing the matched probe selection. The yield of matched probes is estimated as the integral of the $\Delta E'_{\mathrm{probe}}$ distribution, in the range $[\mu - 3\sigma, \mu + 3\sigma]$, where μ and σ are the parameters obtained from a Gaussian fit of the core of the distribution, subtracted by the background yield evaluated in the same range.

The statistical error associated to the tag and matched probe yields are propagated to the efficiency. The photon

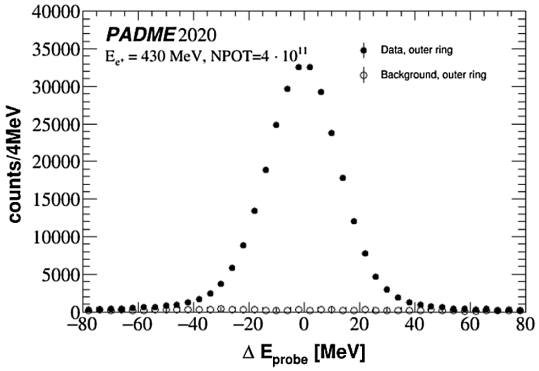

FIG. 8. Distribution of $\Delta E'_{\text{probe}}$ for photons in the outer ring of the radial fiducial region passing the matched-probe selection. The contribution of background is represented by the scaled no-target data.

detection and selection efficiency ϵ_γ measured in the 16 independent regions of the ECAL is shown in Fig. 9, where only statistical errors are considered. The differences from bin to bin are the result of local defects (three inefficient photo-multipliers), asymmetric geometrical acceptance of the PADME detector and inert materials, along with nonuniform background rates in the ECAL. Figure 10

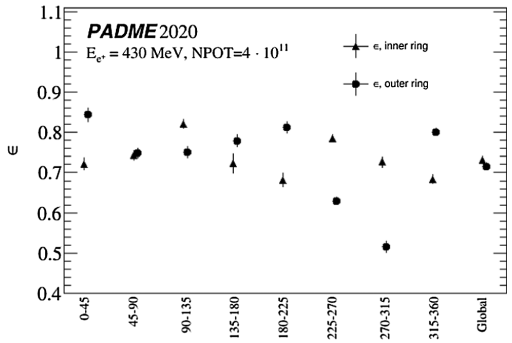

FIG. 9. Tag-and-probe efficiency for eight ECAL slices and two radial regions, showing the global inner and outer efficiency.

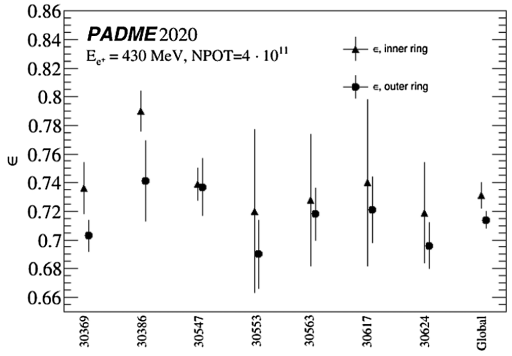

FIG. 10. Single-photon tag-and-probe efficiency for the seven runs and for all runs combined, in the inner and outer radial regions.

shows the single photon efficiency, averaged over ϕ and R, estimated separately for each run in the inner and outer ring of the fiducial region.

The tag-and-probe technique was validated in simulation by applying two closure tests after simulating the ECAL with dead crystals. First, the tag-and-probe efficiency measured in simulation was compared with the truth efficiency after selection cuts. Second, the annihilation cross section measured in simulation, with the same procedure applied in data, was compared to the truth cross section. In both tests the agreement was within 1%.

Owing to the correlation between photon energy and radial position exploited in the tag-and-probe technique, these efficiency measurements are well suited for annihilation photons only, and in general do not apply to photons produced in other physics processes.

The event efficiency $\epsilon_{e^+e^-\to\gamma\gamma}$ is given by the product $\epsilon_{\gamma_1}\epsilon_{\gamma_2}$. The overall single photon efficiency obtained considering tags and matched probes from all slices together is determined to be 0.731 ± 0.009, for photons in the inner ring, and 0.714 ± 0.006, for photons in the outer ring. These values are dominated by the tight selection requirements.

F. Systematic uncertainties

Several contributions to the systematic uncertainty on the cross-section measurement were evaluated.

The signal yield is not expected to be uniform with azimuthal angle because of local detector defects and the presence of the dipole magnet and vacuum vessel. Moreover, in the ECAL the halo of the beam background is offset with respect to the beam axis. As a consequence, the background subtracted in the single-photon selection varies by a factor up to 3 in the inner ring of the fiducial region and up to 7 in the outer ring. The local determination of the photon efficiency by a data-driven method can compensate for these effects. However, residual systematic biases are possible due to the large differences between the average efficiency observed bin-by-bin. The data sample was split in eight azimuthal slices and independent cross-section measurements, one per slice, were performed. The value of the acceptance of a single slice is computed as $A_{g_i} = A_g/8$ and the event efficiency as the product of the local efficiencies relevant for the slice $\epsilon_\gamma(i, j = 1)\epsilon_\gamma(i', j = 2)$, where i is the slice index (i' the index of the opposite slice) and $j = 1(2)$ corresponds to the inner(outer) bin in the slice. The variance of these measurements is found to exceed the expected statistical fluctuations around the weighted average, pointing to the presence of systematic local biases. A systematic uncertainty is therefore assigned to the cross-section measurement, to account for biases in the efficiency from local defects and uneven background distribution, estimated as:

$$\sigma_{\text{eff},\phi} = \sqrt{[\text{RMS}(\sigma_i)]^2 - \delta^2_{\text{stat}}(\langle\sigma\rangle)}. \tag{6}$$

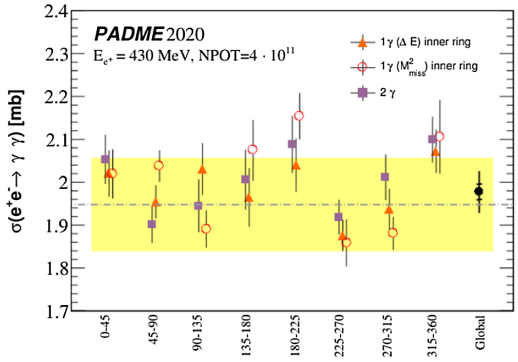

FIG. 11. Cross section for the process $e^+e^- \to \gamma\gamma$ measured in different ECAL azimuthal angle slice (degrees). The error bars represent the statistical error on the measurements. The dotted line represents the QED prediction at NLO estimated with the Babayaga generator [16,17] and the yellow band corresponds to the uncertainty on the number of collisions recorded.

In Eq. (6), σ_i refers to the cross section measured in slice i, $\langle\sigma\rangle$ is the weighted average of the cross-sections and $\delta_{\text{stat}}(\langle\sigma\rangle)$ is its statistical error. This procedure was applied to the measurements, shown in Fig. 11, obtained with three methods: using the two-photon selection, and using the single-photon selection, in the inner ring of the fiducial region, based on either the ΔE or the M^2_{miss} distribution. The average of the three estimates is used as systematic uncertainty on the slice nonuniformity.

The same procedure was applied by splitting the data sample in independent subsamples corresponding to different runs (see Table I). The cross section was measured in each subsample, collecting event candidates from all sectors together, but using a determination of the efficiency for each specific run both for the inner ring (i.e. the set of eight inner bins) and for the outer ring. Deviations in excess of the statistical fluctuations could indicate biases in the efficiency related to the different background conditions determined by the in-time density variation of positrons in beam bunches. Figure 12 shows the measurements for each

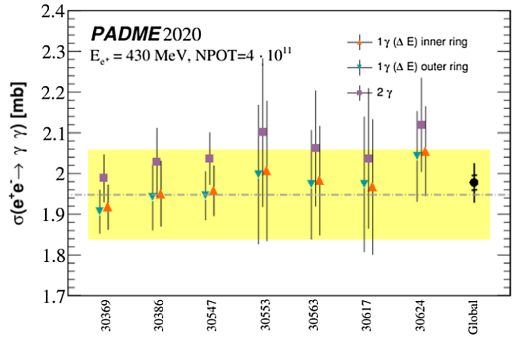

FIG. 12. Cross section for the process $e^+e^- \to \gamma\gamma$ measured in each run separately. The error bars represent the statistical error on the measurements. The dotted line shows the QED prediction at NLO estimated with the Babayaga generator [16,17] and the yellow band corresponds to the uncertainty on the number of collisions recorded.

run together with the measurements considering all runs. Since the fluctuations are fully consistent with the expected statistical error, no systematic uncertainty is assigned.

The background modeling is a potential source of systematic uncertainty. It affects the determination of the efficiency through counting of the number of tag photons as well as yield extraction in the single-photon selection. Since the background component has a different shape in the $\Delta E = E - f(\theta)$ and M^2_{miss} distributions, the procedure applied to assess the resulting systematic error on the cross-section measurement consisted of comparing the cross sections obtained with different methods: two-photon selection, single-photon selection with the yield extracted from the ΔE distribution, and single-photon selection with the yield extracted from the M^2_{miss} distribution. Only photons of the inner radial region were considered, because outer and inner signal photons are related to the same events. The set of the most energetic photons in the two-photon selection is almost a complete overlap with the set of photons of the inner radial region. Therefore, the differences among these three measurements have only a systematic origin, to be ascribed, as aforementioned, to the background modeling. The systematic error is estimated as the root mean square of the three values multiplied by $\sqrt{3}$, to compensate for the suppression factor that would hold in case of statistical independence of the measurements. This procedure gives an error of 0.009 mb.

In addition, the difference between the cross section obtained in the single-photon selection applied in the inner vs. outer rings was considered. The two measurements are based on consistent, but experimentally different, definitions of the fiducial region. Therefore, the difference between the two measurements based on ΔE_{in} and ΔE_{out} can be a source of systematic uncertainty related to the acceptance. This has been assessed as the root mean square of the two values multiplied by $\sqrt{2}$ because exactly the same events are involved. The procedure was repeated with the cross sections measured by single-photon selections in the inner and outer fiducial region based on M^2_{miss}. The average of the two estimates, 0.024 mb, is assumed as a contribution to the systematic error due to acceptance. In addition, the uncertainty on the knowledge of the boundary of the fiducial region (discussed in Sec. IV C) adds another 0.023 mb from the resulting error on the acceptance and another 0.006 mb from the error on the correction A_{mig} accounting for resolution effects. These two uncertainties are treated as fully correlated and when combined with the other sources of error lead to a total systematic uncertainty for the acceptance and event migration of 0.037 mb.

Other contributions to the error on the cross-section measurement come from the uncertainty on the total number of collisions, which originates from the error on the number of POT (N_{POT}), and from the error on the electron surface density in the target, $n_{e/S}$.

TABLE III. Systematic uncertainties on the inclusive annihilation cross-section measurement.

Source	Systematic error (mb)
Azimuthal angle nonuniformity	0.024
Beam conditions	0
Background modeling	0.009
Acceptance and resolution	0.037
Total	0.045
N_{POT}	0.079
Target electron surface density	0.073
Total	0.110

The relative uncertainty on N_{POT} (see Sec. IV) is 4% and dominated by the uncertainty on the absolute charge calibration of the active target response. The absolute scale of the charge response was cross-calibrated with a lead-glass Cherenkov calorimeter working in full-containment mode. Intensities from 5×10^3 up to 35×10^3 positrons per bunch were considered, at the energy of 430 MeV. In the data-taking campaign of fall 2020 the beam spot was focused on a few target strips in both directions and an *ad-hoc* nonlinear calibration was necessary to determine the number of POT, reaching a precision of 4%. This uncertainty was derived by comparing across several runs the measurement of the number of POT per bunch from the diamond target, averaged over the run, with measurements of the beam intensity per bunch performed at the start and at the end of the run with the calibration calorimeter.

The uncertainty on $n_{e/S}$ (reported in Sec. IV) is dominated by the error on the diamond target thickness, $\sigma_d = 0.0036$ mm. The average thickness of the active target was measured, after assembly, using an optical profilometer with a 1 μm spatial resolution as the difference with respect to a supporting surface. Because of the roughness of the unpolished diamond surface (Ra = 3.2 μm according to the manufacturer), a correction needs to be applied. This is obtained by comparing the result of the same procedure with precision mass and surface measurements on other similar CVD diamond samples. The error accounts for the statistical uncertainty on the measurements performed with the profilometer, but is dominated by the systematic component assessed as one half of the roughness related correction.

All sources of systematic errors are summarized in Table III.

G. Inclusive $e^+e^- \to \gamma\gamma$ cross-section results

The local variations in the photon efficiency lead to separate measurements of the cross section in eight independent azimuthal angle slices of the ECAL by exploiting the granularity of the efficiency measurement. Eventually, the measurements are statistically combined in a weighed average.

The cross-section measurements from the three methods (two-photon selection, and single-photon selection in the inner fiducial region exploiting ΔE and M^2_{miss}) can be considered equivalent, since they are based on the same sample of annihilation events. Therefore, they are combined in a simple average, giving the final inclusive cross-section measurement:

$$\sigma_{e^+e^-\to\gamma\gamma}[\mathrm{PADME}] = 1.977 \pm 0.018\ (\mathrm{stat}) \pm 0.045\ (\mathrm{syst}) \pm 0.110\ (n.\mathrm{collisions})\ \mathrm{mb}. \quad (7)$$

The systematic error is the combination of the experimental systematic uncertainties described in Sec. IV F. The error coming from the uncertainty on the total number of collisions is quoted separately.

The measurement is compatible with the QED prediction at NLO, estimated with the Babayaga generator [17],

$$\sigma_{e^+e^-\to\gamma\gamma}[\mathrm{Theory}] = 1.9478 \pm 0.0005\ (\mathrm{stat}) \pm 0.0020\ (\mathrm{syst})\ \mathrm{mb} \quad (8)$$

for the inclusive in-flight annihilation cross section at the positron energy of $E_{e+} = 432.5$ MeV. In Eq. (8), the statistical error comes from the statistics of the MC simulation generation and the systematic error is a conservative estimate of higher-order corrections. Figure 13 shows a comparison of the two-photon annihilation cross section measured by PADME with the theoretical predictions and with other measurements performed in the past at similar energy scales.

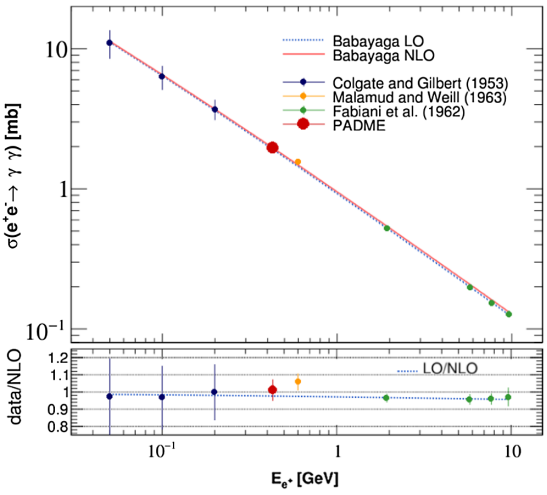

FIG. 13. Comparison between our experimental result and theory predictions, at the leading order and next-to-leading order approximation, for the positron annihilation cross section in flight as a function of the positron energy. The PADME measurement is superimposed on earlier measurements. Data to theory ratios are shown in the bottom pad.

V. SUMMARY

The inclusive annihilation cross section of 432.5 MeV positrons with atomic electrons in carbon leading to two-photon final states has been measured with the PADME experiment. The high-accuracy measurement is performed using a high-granularity electromagnetic calorimeter made of BGO crystals and a pulsed beam with about 27,000 positrons per bunch. A tag-and-probe technique was applied to measure the efficiency for annihilation photons as determined by detector defects and asymmetries in the acceptance of the apparatus, reconstruction efficiency, physics and beam related background. The PADME result on the Run II data subset is

$$\sigma_{e^+e^-\to\gamma\gamma} = (1.977 \pm 0.018_{\text{stat}}, \pm 0.119_{\text{syst}})\ \text{mb}$$

in good agreement with NLO QED predictions.

The PADME measurement exploits the reconstruction of the photon pair for the first time with beam energies below 1 GeV. Previous results [4,5] were based on the measurement of the rate of positron disappearance, which might receive contributions from beyond-standard-model processes leading to undetected final states. The PADME measurement, instead, is free from assumptions about new physics producing invisible final states.

The experimental and analysis techniques reported here pave the way for accurate SM QED measurements and searches for new physics in positron annihilation in flight, such as MeV mass scale dark photons and axions.

ACKNOWLEDGMENTS

The PADME collaboration would like to thank all LNF staff that gave support to the experiment in any phase. In particular all LINAC operators, BTF staff members and the personnel of the vacuum service of the accelerator division. All the technicians of the research division, and in particular C. Capoccia, E. Capitolo, S. Ceravolo. The collaboration wishes to acknowledge the continuous support from the technical personnel from INFN Lecce and Dipartimento di Matematica e Fisica of Università del Salento, in particular R. Assiro, A. Miccoli, and C. Pinto. A special thank goes to C. Carloni Calame for the precious help in estimating the NLO cross section and kinematics using the Babayaga generator. This paper benefited by a support from TA3-LNF as part of the STRONG-2020 project—EU Grant Agreement 824093.

[1] M. Raggi and V. Kozhuharov, Proposal to search for a dark photon in positron on target collisions at DAΦNE linac, Adv. High Energy Phys. **2014**, 1 (2014).
[2] J. Alexander *et al.*, Dark sectors 2016 workshop: Community report, arXiv:1608.08632.
[3] D. J. Miller, The physics of the dark photon: A primer, Contemp. Phys. **62**, 110 (2021).
[4] S. A. Colgate and F. C. Gilbert, Electron-positron annihilation in flight, Phys. Rev. **89**, 790 (1953).
[5] E. Malamud and R. Weill, Electron-positron annihilation in flight at 600 MeV, Il Nuovo Cimento **27**, 418 (1953).
[6] F. Fabiani, M. Fidecaro, G. Finocchiaro, G. Giacomelli, D. Harting, N. H. Lipman, and G. Torelli, Positron-electron annihilation in flight between 2 and 10-GeV, Nuovo Cimento **25**, 655 (1962).
[7] B. Buonomo, L. G. Foggetta, and G. Piermarini, New gun implementation and performance of the DAΦNE linac, in *Proceedings of the 6th International Particle Accelerator Conference* (JACoW Publishing, Richmond, VA, 2015).
[8] P. Valente *et al.*, Linear accelerator test facility at lnf conceptual design report, arXiv:1603.05651.
[9] F. Oliva, Operation and performance of the active target of PADME, Nucl. Instrum. Methods Phys. Res., Sect. A **958**, 162354 (2019).
[10] P. Albicocco *et al.*, Characterisation and performance of the padme electromagnetic calorimeter, J. Instrum. **15**, T10003 (2020).
[11] E. Leonardi, M. Raggi, and P. Valente, Development and test of a DRS4-based DAQ system for the PADME experiment at the DAΦNE BTF, J. Phys. Conf. Ser. **898**, 032024 (2017).
[12] P. Albicocco *et al.*, Commissioning of the PADME experiment with a positron beam, J. Instrum. **17**, P08032 (2022).
[13] F. Bossi *et al.*, The PADME beam line Monte Carlo simulation, J. High Energy Phys. 09 (2022) 233.
[14] S. Agostinelli *et al.*, GEANT4—A simulation toolkit, Nucl. Instrum. Methods Phys. Res., Sect. A **506**, 250 (2003).
[15] A. Belyaev, N. D. Christensen, and A. Pukhov, Calchep 3.4 for collider physics within and beyond the standard model, Comput. Phys. Commun. **184**, 1729 (2013).
[16] C. M. Carloni Calame, G. Montagna, O. Nicrosini, and F. Piccinini, The babayaga event generator, Nucl. Phys. B, Proc. Suppl. **131**, 48 (2004).
[17] G. Balossini, C. Bignamini, C. M. C. Calame, G. Montagna, O. Nicrosini, and F. Piccinini, Photon pair production at flavour factories with per mille accuracy, Phys. Lett. B **663**, 209 (2008).